To be submitted to Chemical Geology

Simultaneous U-Pb isotope and trace element analysis of columbite and zircon by laser ablation ICP-MS: implications for geochronology of pegmatite and associated ore deposits

Xiao-Dong Deng[a,b], Jian-Wei Li[a,b,*], Xin-Fu Zhao[c], Zhao-Chu Hu[a], Hao Hu[b], David Selby[d], Zorano S de Souza[e]

[a] State Key Laboratory of Geological Processes and Mineral Resources, China University of Geosciences, Wuhan 430074, China

[b] Faculty of Earth Resources, China University of Geosciences, Wuhan 430074, China

[c] Department of Earth Sciences, The University of Hong Kong, Hongkong SAR, China

[d] Department of Earth Sciences, University of Durham, Durham DH1 3LE, United Kingdom

[e] Department of Geology, Universidade Federal do Rio, Grande do Norte, Natal 1524, Brazil

<u>* Corresponding author:</u>

E-mail: jwli@cug.edu.cn

Phone: +86 1387111 2076

Fax: +86 27 6788 5096

Abstract

U-Pb isotopes and trace elements of columbite and zircon from an early Cretaceous pegmatite dike in the Xiaoqinling district, North China Craton, were simultaneously analyzed using laser ablation inductively coupled plasma mass spectrometry (LA-ICP-MS) to illustrate that columbite is a more robust U-Pb geochronometer compared to zircon when they were attacked by post-dike hydrothermal fluids. Columbites have high W, Ti, U, Th, and REEs contents and yield concordant U-Pb ages of 143 ± 1 Ma (1σ, n = 10) that is interpreted as the emplacement age of the pegmatite dike. In contrast, zircons from the same dike show three distinct age populations. Nine of the seventeen zircons analyzed have textural features typical of magmatic zircon and yield a weighted mean $^{206}Pb/^{238}U$ age of 143 ± 1 Ma (1σ, n = 9), identical to that of columbite and thus constrain the timing of the pegmatitic magmatism. The second population of zircons is characterized by corroded and zoned textures with geochemical affinities of magmatic zircons. These zircons have a weighted mean $^{207}Pb/^{206}Pb$ age of 1879 ± 30 Ma (1σ, n = 5) and are considered to be inherited grains derived from Paleoproterozoic basement rocks that are widely distributed in the Xiaoqinling district. A third zircon population is characterized by abundant porosities and Th-U-rich mineral inclusions (e.g. thorite, uranium oxides), and have a younger U-Pb age of 127 ± 3 Ma (1σ, n = 3). These younger zircons have elevated Hf, Ca, P, Nb, Ta, and Ti contents and much higher Th/U, LREE/MREE, and LREE/HREE ratios than the 143 Ma zircons. The textural and geochemical data for these grains indicate that they are products of hydrothermal alteration of precursor

zircons formed during the crystallization of the pegmatitic magmas, presumably caused by pervasive hydrothermal flow that led to formation of numerous early Cretaceous gold deposits in the Xiaoqinling district. The results from this study demonstrate that columbite is resistant to post-magmatic hydrothermal alteration that can disturb the U-Pb isotopes in zircon. Consequently, columbite could be a more robust U-Pb geochronometer than zircon when they have been affected by subsequent hydrothermal activity, and therefore can be widely used for precisely dating of pegmatites and associated ore deposits.

Key Words: Columbite; zircon; pegmatite; U-Pb dating; LA-ICPMS

1. Introduction

Pegmatites commonly form at the waning stage of magma evolution by fractional crystallization of volatile-rich magmas (London, 2005), and provide important sources for strategic metals (e.g. Li, Be, Cs, Ta, Nb, and rare earth elements (REEs); Linnen et al., 2012), as well as high-quality gem minerals (e.g. beryl, tourmaline, topaz, spodumene, and spessartine; Simmons et al., 2012). Ages of pegmatite have traditionally been determined by U-Pb geochronology of zircons formed during the crystallization of pegmatitic magmas (e.g. Romer, 1997; Wang et al., 2007). However, zircons in pegmatite commonly have high U and Th contents that may cause radioactive damage to the mineral structure, and thus affect the resistance of zircon grains due to selective loss or gain of U, Th, and Pb (Geisler et al., 2002). Hydrothermal alteration is an additional factor that may produce incongruent dissolution and re-crystallization of zircon, resulting in disturbance of the U-Pb isotope systematics in the mineral (Geisler et al., 2007; Wang et al., 2007; Kusiak et al., 2009). The aforementioned factors, therefore, may hinder the ability to precisely date the formation age of pegmatites and associated ore deposits by U-Pb zircon geochronology.

Columbite is another common accessory mineral in pegmatites (Černý and Ercit, 1989), and occurs widely in granite-related hydrothermal Sn, W, and REEs deposits (Zhang et al., 2001; Zhang et al., 2003; Lerouge et al., 2007; Beurlen et al., 2008). It is also present in alkaline and carbonatitic intrusions (Möller, 1989). This mineral usually has relatively high U but low common lead contents, and therefore can be an ideal target for U-Pb dating of pegmatites and related mineral deposits (Romer and Wright, 1992; Romer and Smeds, 1994; Romer and Lehmann, 1995; Romer and Smeds, 1996; Romer and Smeds, 1997). Smith et al. (2004) and Melcher et al. (2008) successfully dated, for the first time, columbite from pegmatites in the Superior Province of Canada and Africa (Ghana, Rwanda, Congo, and Namibia), using LA-MC-ICP-MS and LA-ICP-MS methods, respectively. In this paper, we present a comparative geochemical and U-Pb geochronology study of columbite and zircon from a pegmatite dike in the Xiaoqinling district, North China Craton (NCC). Our results reveal that some zircons from this pegmatite have been intensively affected by post-pegmatite hydrothermal alteration and yield ages that are significantly younger than the true emplacement age of the dike. In contrast, the coexisting columbites survived hydrothermal alteration and provide reliable chronological constraints on the pegamtitic magmatism. The present study therefore highlights the utilization of columbite as a more robust U-Pb geochronometer to precisely date the formation of pegmatites and associated ore deposits.

2. Geological setting

The Xiaoqinling district is located along the southern margin of the NCC and is bounded by the Taiyao Fault to the north and the Xiaohe Fault to the south (Fig. 1). The district is dominated lithologically by amphibolite facies metamorphic rocks of the late Archean to early Paleoproterozoic Taihua Group that consist mainly of amphibolite, gneiss, and migmatite. The ages of the Taihua Group have been constrained at 2.6 to 2.3 Ga by *in situ* zircon U-Pb dating (Li et al., 2007; Xu et al., 2009). A number of plutonic intrusions, ranging in composition from monzogranite through biotite granite to pegmatitic granite and pegmatites, were emplaced into the Taihua Group (Figs. 1 and 2). The biotite granite, which was emplaced along the Xiaohe Fault, has zircon U-Pb ages of ~1.7 Ga (Nie et al., 2001), whereas samples of pegmatitic granite have zircon U-Pb ages of ~2.0 Ga (Hu and Lin, 1989). These age constraints reveal late Paleoproterozoic magmatism in the area, as recently confirmed by geochronological studies of mafic dikes spatially related to the pegmatitic granite (Fig. 2; Li et al., 2012a). The monzogranites consist of, from west to east, the Huashan, Wenyu, and Niangniangshan plutons (Fig. 1), which have zircon U-Pb ages of ~146 Ma, 141-138 Ma, and 143-135 Ma, respectively (Mao et al., 2010; Li et al., 2012a). Widesparead diabase dikes in the distinct were formed in two episodes at ~1.9

to 1.8 Ga and 140-125 Ma (Wang et al., 2008; Bi et al., 2011; Li et al., 2012a). The Xiaoqinling district contains numerous gold deposits, mostly occurring in the flanks of three NWW-oriented folds (Fig. 1). Comprehensive geochronological studies (molybdenite Re-Os and mica $^{40}Ar/^{39}Ar$) indicate that gold mineralization occurred in the range of 154 to 118 Ma (Li et al., 2012a, 2012b).

Numerous pegmatite dikes intrude the Taihua Group and the late Paleoproteorozic pegmatitic granite (Fig. 2). These pegmatites can be classified into two main groups: G1 dikes generally strike 275-300º (Fig. 2) and typically contain K-feldspar, quartz, biotite, and tourmaline. These pegmatites are though to be related to regional migmatization and magmatism at 2.0-1.8 Ga (Hu and Lin, 1989; Li et al., 2007). G2 pegmatite dikes generally strike northeast and surround the Wenyu pluton (Fig. 2). They mostly occur as relatively flat bodies, 1-3 m wide and 5-100 m long, that crosscut diabase dikes and pegmatitic granites (Figs. 3A and B). G2 pegmatites consist mainly of albite and quartz, with minor amounts of muscovite, biotite, and garnet. Accessory minerals include zircon, columbite, apatite, monazite, magnetite, and thorite. Age constraints on the G2 pegmatites are lacking. The present study focuses on a G2 pegmatite dike.

3. Sample description

Samples used for U-Pb geochronology were collected from a G2 pegmatite emplaced in the southern margin of the Wenyu pluton (Fig. 2). The samples consist mainly of albite (50 vol.%), quartz (43 vol.%), muscovite (4 vol.%), biotite (2 vol.%), and garnet (1 vol.%) (Fig. 4A). Quartz ranges in size from 0.3-2 cm, whereas albite crystals are commonly 1-5 cm across. Large crystals are common in the inner parts of the dike. Garnets are characteristically fine-grained (generally <0.2 cm) (Fig. 4A). Hydrothermal sericite is locally present along cleavages and micro-fractures in albite (Fig. 4B). Columbite, zircon, monazite, and thorite are common accessory minerals (Figs. 5).

The geochemical characteristics of the sampled pegmatite are summarized in the Supplementary Data (Tables S.1 and S.2). Samples are slightly peraluminous with an average aluminum-saturation index [Al/ (2 (Ca-1.67P) +Na+K] of 1.08 (0.97-1.21). They are enriched in incompatible elements including Rb (689-1179 ppm), Th (52.3-85.5 ppm), U (20.2-39.5 ppm), Nb (328-530 ppm), Ta (9.8-17.1 ppm), Zr (142-185 ppm), Hf (12.9-17.4 ppm), but have very low MgO (0.03–0.06 wt%), Sr (2.35-7.30 ppm) and Ba (5.63-18.2 ppm) (Table S.2). The low K/Rb values (35–40) suggest that the pegmatite was crystallized from a highly fractionated magma. In addition, the rocks have ΣREEs ranging from 99.8 to 173.9 ppm, with significant negative Eu anomalies (Eu* = 0.013-0.03; Table S.1 and S.2).

4. Analytical methods

Thin sections of the samples were first investigated under transmitted-light to determine the mineralogy, textural relationships, and extent of post-emplacement hydrothermal alteration. Zircon and columbite were separated using conventional heavy-liquid and magnetic methods, and then handpicked under a binocular microscope. Representative grains were mounted in epoxy and polished to expose their interiors. The polished grains were examined using optical microscopy and scanning electron microscopy (SEM) equipped with energy dispersive spectrometry (EDS). Back-scattered electron (BSE) and cathodoluminescence (CL) images were used to characterize the morphology and internal structure of zircon and columbite, using a FEI Quanta200 environmental SEM and a MonoCL detector on a JXA-8100 electron microscope in the State Key Laboratory of Geological Processes and Mineral Resources (GPMR), China University of Geosciences, Wuhan.

Major element analyses of columbite were carried out on a JAX 8230 Superprobe at the Center for Material Research and Analysis, Wuhan University of Technology. Operating conditions included an acceleration voltage of 20 kV, sample current of 30 nA, and a beam diameter of 5 μm. The counting time was 30 s on-peak and 10 s for off-peak background measurements. The following standards were used: $Ca_5(PO_4)_3F$ (Ca), $(Mn,Ca)SiO_3$ (Mn), Fe_2O_3 (Fe), Nb (Nb), Ta (Ta), TiO_2 (Ti), U (U), Sc (Sc), SnO_2 (Sn), W (W), ZrO_2 (Zr), and Y_5PO_{14} (Y).

U-Pb isotopes and trace elements of zircons and columbites were simultaneously analyzed at GMPR using an Agilent 7500a ICP-MS apparatus coupled with a GeoLas 2005 laser-ablation system with a DUV 193 nm ArF-excimer laser (MicroLas, Germany). Detailed analytical procedures and data reduction are available in Liu et al. (2008; 2010a) and are briefly summarized here. A spot size of 32 μm was used for all analyses. Argon was used as the make-up gas and mixed with the carrier gas (helium) via a T-connector before entering the ICP. Nitrogen was added into the central gas flow (Ar + He) of the Ar plasma to decrease the detection limit and improve precision, which increases the sensitivity for most elements by a factor 2 to 3 (Hu et al., 2008). Each analysis incorporated a background acquisition of 20-30 s (gas blank) followed by 50 s data acquisition. Zircon 91500 was used as a calibration standard for mass discrimination and U-Pb isotope fractionation. Time-dependent drift of U-Th-Pb isotopic ratios were corrected using a linear interpolation (with time) for every five analyses according to the variations of 91500 (Liu et al., 2010b). Preferred U-Th-Pb isotopic ratios used for 91500 are from Wiedenbeck et al. (1995). The precision and accuracy of U-Pb dating with this technique have been evaluated by comparison with TIMS data of zircon standard GJ-1 (Jackson et al., 2004). In this study, the minor, non-radiogenic isotope ^{204}Pb was analyzed as a monitor of common lead, and the signals of the radiogenic isotopes ^{206}Pb, ^{207}Pb, and ^{208}Pb were corrected in proportion to their relative abundances in common lead (Stacey and Kramers, 1975). The isotope ^{202}Hg was measured simultaneously and used to correct for the ^{204}Hg isobaric interference on ^{204}Pb. This approach has been shown to be effective in correcting minor common Pb (Storey et al., 2006; Li et al., 2010). Trace elements were calibrated against multiple-reference standards (NIST SRM610 and BCR-2G) combined with internal standardization (Liu et al., 2010b). Off-line selection and integration of background and analyzed signals, and time-drift correction and quantitative calibration for trace element analyses and U-Pb dating were performed by *ICPMSDataCal* (Liu et al., 2008; Liu et al., 2010a). Uncertainties of preferred values for the external standard 91500 were propagated into the ultimate results of the samples. Concordia diagrams and weighted mean calculations were made using Isoplot/Ex_ver3 (Ludwig, 2003).

5. Results

5.1. Geochemistry of columbite

Columbite occurs as euhedral grains enclosed in albite, quartz, or garnet (Figs. 5A-C). The mineral grains are 20-400 μm in diameter, without zoning and mineral inclusions (Fig. 5D). Twelve electron microprobe analyses on 5 grains reveal relatively homogeneous compositions, with 10.27-12.67 wt.% MnO (excepting one analysis at 17.17 wt.%), 2.87-9.87 wt.% FeO, 68.13-73.96 wt.% Nb_2O_5, and 1.30-7.56 wt.% Ta_2O_5 (Table 1). In addition, the mineral contains significant amount of TiO_2 (1.12-4.76 wt.%), WO_3 (up to 4.26 wt.%), UO_2 (0.05-1.35 wt.%), and Y_2O_3 (0.35-1.26 wt.%). Other minor elements include SnO_2 (up to 0.17 wt.%), ZrO_2 (up to 0.79 wt.%), and Sc_2O_3 (up to 0.39 wt.%). In the columbite-tantalite quadrilateral diagram, the analyses plot in the manganocolumbite field (Fig. 6A). The composition show a slight deviation from the ideal trend defined by the substitution: $(Fe, Mn)^{2+}$ + $2(Nb, Ta)^{5+} = 3(Ti, Sn, U, Sc, Zr)^{4+}$ (Fig. 6B; Černý et al., 1985), likely due to the presence of significant amounts of other elements (e.g., Th, Y, and REE) in the mineral. Titanium correlates positively with U, Sc, Zr, and Sn (Figs. 7A-D), indicating that these cations behave like Ti during crystallization of columbite. The tetravalent cations combined (Ti+Sn+U+Zr+Sc) decrease with increasing Ta/(Ta+Nb) fractionation (Fig. 7E), indicating that these cations are preferentially partitioned into earlier-formed minerals such as zircon and Nb-rich columbite (Černý et al., 1986; Ercit, 1994; Linnen and Keppler, 1997). Columbite also contains variable WO_3 (up to 4.26 wt.%) that correlates positively with Ta (Fig. 7F), suggesting that W behaves similarly to Ta during crystallization of this mineral. The W/Ta ratios are approximately 1:2 (Fig. 7F), implying that these elements may be present as WTa_2O_8 solid solution or inclusions in columbite (Zhang et al., 2003).

Trace element concentrations of the columbite are present in Table 2. The contents of U range from 1713 to 19143 ppm, consistent with the EMP results (Table 1). Thorium concentrations are between 36.7 and 1186 ppm, and correlate positively with U (Fig. 7G). The Th *vs* U relation suggests that F, rather than Cl and/or CO_2, was the dominant complexing agent both for Th and U (Keppler and Wyllie, 1990). This in turn indicates that the columbite likely formed from F- and Li-dominated fluid as shown in the Ta/(Ta+Nb) *vs* Mn/(Mn+Fe) diagram (Fig. 6A). In addition, the columbite is relatively enriched in MREE and HREE, with LREE/MREE and LREE/HREE ratios of 0.3-0.5 and 0.7-1.1, respectively. The total REE contents correlate positively with U (Fig. 7H), indicating that REE may enter the columbite structure by a euxenite-type substitution mechanism ($A^{2+}+B^{5+} \rightarrow REE^{3+}+ Ti^{4+}$; Graupner et al., 2010). Chondrite-normalized REE patterns (Fig. 7I) are characterized by significant enrichment of MREE, prominent negative Eu anomalies (Eu* = 0.002-0.008), and weak positive Ce anomalies (Ce* = 0.92-4.07).

5.2. Geochemistry of zircon

Based on their morphology and textures, zircons from the pegmatite can be classified into three types. Type 1 consists of euhedral to subhedral grains that are 100-200 μm long with length/width ratios of 1-2. They are semitransparent, pale to gray, homogenous, and characterized by dark cores and irregular magmatic overgrowth zones in CL images (Figs. 8A and B). These zircons have low Hf (1.1-1.8 wt.%), P (144-860 ppm), Ca (<80.5 ppm), Ti (1.1-3.3 ppm), Nb (1.2-25.4 ppm) and Ta (1.2-9.8 ppm) with Nb/Ta ratios of 1.0-2.6 (Table 3; Figs. 9A-C). Thorium and U concentrations are relatively low, with Th/U ratios of 0.2-0.6 (Fig. 9D). In addition, they have relative low LREE/HREE, LREE/MREE, and MREE/HREE ratios ranging from 0.01-0.04, 0.05-0.19, and 0.20-0.28, respectively (Figs. 9E and F). Chondrite-normalized REE patterns display obvious negative Eu anomalies and variable Ce anomalies (Fig. 9G). In the Ce* *vs* $(Sm/La)_N$ and $(Sm/La)_N$ *vs* La diagrams, type 1 zircons fall in or close to the magmatic zircon field as defined by Hoskin (2005) (Figs. 9H and I).

Type 2 zircons consist of euhedral to subhedral grains that are 200-400 μm long with aspect ratio of 2:1 to 4:1. Most grains are brown to dark, homogenous (Figs. 8C), and black in CL images (Figs. 8D). These grains has abnormally high Hf (4.1-20.8 wt.%) and relatively low P (284-1260 ppm), Ca (16-703 ppm), Ti (1.9-9.2 ppm), Nb (32-201 ppm) and Ta (28-137 ppm) with Nb/Ta ratios of 0.6-1.8 (Table 3; Figs. 9A-C). Thorium and U concentrations are extremely variable, ranging from 261-15800 ppm and 3270 to 71182 ppm, respectively (Table 3), with low Th/U ratios at 0.1-0.2 (Fig. 9D). Type 2 zircons have relatively low LREE/HREE (0.04-0.19) and LREE/MREE

(0.03-0.13) ratios, but high MREE/HREE ratios (0.35-2.68) (Figs. 9E and F). Chondrite-normalized REE patterns display strong negative Eu anomalies (Eu* = 0.003-0.069) and variable Ce anomalies (Ce* = 0.88-31.5) (Fig. 9G). In the Ce* *vs* $(Sm/La)_N$ and $(Sm/La)_N$ *vs* La diagrams, the type 2 zircons plot in the transitional area between magmatic and hydrothermal zircon, but closer to the magmatic field (Hoskin, 2005) (Figs. 9H and I).

Type 3 zircons are similar in morphology to Type 2 varieties, but the former are characterized by high porosity and abundant mineral inclusions (Fig. 8E). These zircons have high Hf (3.3-6.3 wt.%), P (978-1895 ppm), Ca (1356-4404 ppm), Ti (16-45 ppm), Nb (225-852 ppm) and Ta (63-70 ppm) with Nb/Ta ratios of 3.2-13.5 (Table 3, Figs. 9A-C). They contain unusually high Th and U, ranging from 10161-24074 ppm and 12879-41724 ppm, respectively (Table 3), corresponding to Th/U ratios of 0.6-0.9 (Fig. 9D). Type 3 zircons have relative high LREE/HREE, LREE/MREE, and MREE/HREE ratios, ranging from 0.17-0.86, 0.19-0.69 and 0.90-1.25, respectively (Figs. 9E and F). Chondrite-normalized REE patterns show significant negative Eu anomalies (Eu* = 0.015-0.046) and weak positive Ce anomalies Ce (Ce* = 1.05-1.49) (Fig. 9G). In the Ce* *vs* $(Sm/La)_N$ and $(Sm/La)_N$ *vs* La diagrams, the type 3 zircons plot very close to the hydrothermal zircon field (Figs. 9H and I).

5.3. U-Pb ages of columbite and zircon

The U-Pb data of zircon and columbite are summarized in Table 4 and graphically illustrated in Figure 10. Ten spot analyses on 10 columbite grains are concordant or nearly concordant (Table 4; Fig. 10A) and have a weighted mean $^{206}Pb/^{238}U$ age of 143 ± 1 Ma (1σ, MSWD = 0.54). A total of 17 analyses were made on 15 zircon grains, all yielding concordant or nearly concordant U-Pb ages (Table 4; Fig. 10B). Five analyses on cores and rims of Type 1 zircon have $^{207}Pb/^{206}Pb$ ages ranging from 1873 ± 38 to 1883 ± 33 Ma, with a weighted mean of 1879 ± 30 Ma (1σ, MSWD = 0.02). Nine Type 2 zircons have $^{206}Pb/^{238}U$ ages of 142 ± 1 to 145 ± 6 Ma, with a weighted mean $^{206}Pb/^{238}U$ age of 143 ± 1 Ma (1σ, MSWD = 0.24). The remaining 3 grains of Type 3 are also concordant or marginally concordant and yield reproducible $^{206}Pb/^{238}U$ age of 125 ± 3 to 128 ± 2 Ma, with a weighted mean of 127 ± 3 Ma (1σ, MSWD = 0.35).

6. Discussion

6.1. Interpretation of columbite and zircon U-Pb ages

Columbite within the pegmatite is commonly included in and texturally equilibrated with albite, quartz, and garnet (Figs. 5A-C), indicating cogenetic growth of these minerals from the pegmatitic magma. This view is confirmed by the high Nd, REE and U abundances in columbite (Table 2; Ercit, 1994). In addition, chondrite-normalized REE patterns of columbite are characterized by HREE≤MREE and the presence of prominent negative Eu anomalies (Fig. 7I), consistent with crystallization of the mineral from highly fractionated magma (Graupner et al., 2010). The petrographic and geochemical data, therefore, suggest a magmatic origin for the columbite and thus its U-Pb age (143 ± 1 Ma) can be reliably considered as the crystallization age of the mineral and of the host pegmatite.

In contrast, zircons extracted from the same pegmatite dike have much more complicated U-Pb age patterns. Type 1 zircons have a $^{207}Pb/^{206}Pb$ age of 1879 ± 30 Ma. They have dark cores and irregular oscillatory zones (Fig. 8B) and Th/U ratios (0.16-0.64) that are typical of magmatic zircon. Their REE patterns (Fig. 9G) are also consistent with a magmatic origin (Hoskin and Schaltegger, 2003). In the Ce* *vs* $(Sm/La)_N$ and $(Sm/La)_N$ *vs* La diagrams (Figs. 9H and I), Type 1 zircons all plot in or proximal to the magmatic zircon field (Hoskin, 2005). Their $^{207}Pb/^{206}Pb$ age is comparable with that of zircons from many Paleoproterozoic diabase and pegmatite dikes in the Xiaoqinling district (1.9-1.8 Ga, Li et al., 2007; Bi et al., 2011; Li et al., 2012a). Taken together, Type 1 zircons are interpreted as inherited grains.

Type 2 zircons have abnormally high Hf contents (up to 20.8%), which is consistent with a highly differentiated pegmatitic source (Pupin, 2000). They are characterized by enrichment of MREE relative to HREE (MREE/HREE = 0.35-2.68; Table 3), indicating a magmatic source with garnet as a residue or separation of garnet during the evolution of the magma (Rubatto, 2002); the presence of abundant garnet in the pegmatite (Fig. 4A) favors the second possibility. Type 2 zircons display strong negative Eu anomalies (Eu* = 0.003-0.069) that resemble the whole-rock samples of the pegmatite dike (Eu* = 0.013-0.030, Table S.2), implying a close relationship between zircon and the pegmatite. In the Ce* *vs* $(Sm/La)_N$ and $(Sm/La)_N$ *vs* La diagrams (Figs. 9H and I), Type 2 zircons plot between the hydrothermal and magmatic zircon fields, but closer to the magmatic field, confirming that they grew from a hydrous silicic melt (London, 2005). It is thus concluded that Type 2 zircons crystallized from volatile-rich pegmatitic magmas. Consequently, the weighted mean $^{206}Pb/^{238}U$ age (143 ± 1 Ma) of the Type 2 zircons is interpreted as the emplacement age of the pegmatite. This age is consistent with the emplacement age of the Wenyu monzogranite pluton and a dioritic enclave in the pluton (141 ± 2 and 141 ± 1 Ma; Li et al., 2012a), indicating that the pegmatite dike may have been derived from a precursor magma represented by the Wenyu pluton.

Type 3 zircons contain abundant mineral inclusions (e.g. thorite, uranium oxides) and high concentrations of Ca, P, Nd, Ta, and LREE (Table 3; Figs. 9A-D), features commonly observed in hydrothermal zircons (Geisler et al., 2007; Kusiak et al., 2009). These zircons also have significantly higher Nb/Ta and Th/U ratios compared to the Type 2 equivalents, suggesting that Type 3 zircons may have resulted form re-equilibration of the Type 2 varieties with a post-crystallization Nb- and Th-rich fluid. In the Ce* *vs* $(Sm/La)_N$ and $(Sm/La)_N$ *vs* La diagrams (Figs. 9H and I), Type 3 zircons plot in the vicinity of the hydrothermal zircon field, distinctly different from Type 2 grains, indicating they are hydrothermal in origin. On the other hand, Type 3 zircons are similar in morphology to the Type 2 grains and have high Hf contents (up to 6.3 wt.%), suggesting that Type 3 zircons likely formed by hydrothermal alteration of Type 2 zircons. The presence of sericite in albite (Fig. 4B) is consistent with such hydrothermal processes. The ages of Type 3 zircons (125 ± 3 to 128 ± 2 Ma) overlap the ages of pervasive hydrothermal alteration and gold deposition throughout the

Xiaoqinling district that peaked at 130-125 Ma (Li et al., 2012a, 2012b). This indicates that some zircons from the pegmatite have been affected by subsequent hydrothermal activities, presumably related to the district-wide hydrothermal flow and gold mineralization. Collectively, it is concluded that columbite U-Pb ages provide direct and reliable constraints on the timing of G2 pegmatite formation in the Xiaoqinling district, whereas zircons from the same dike have been variably affected by later hydrothermal activities that complicated the age patterns of zircons and therefore caused problems in unequivocally dating the pegmatite.

6.2 Implications for geochronology of pegmatite and associated ore deposits

The U-Pb zircon geochronometer is a powerful tool for dating igneous rocks including pegmatite bodies (Romer, 1997; Wang et al., 2007). However, the present and previous studies demonstrate that potential problems may exist in zircon U-Pb dating of pegmatite: (1) Pegmatite bodies often contain significant amounts of inherited zircon (Romer, 1997; Wang et al., 2007; Ghosh et al., 2008; Marsh et al., 2012), due to the low temperatures of pegmatitic magmas (Watson and Harrison, 1983; Hanchar and Watson, 2003; London, 2005). The presence of such material would complicate the age distribution (Romer and Wright, 1992; Romer, 1997) and lead to erroneous results. (2) Zircons in pegmatite often have unusually high U and Th concentrations, as exemplified by the present sample (7.1 wt.% U and 2.4 wt.% Th; Table 3). Such extremely high U and Th may cause metamictic damage to the zircons and thus promote a matrix-mismatch effect between the zircon standard and unknown during U-Pb isotopic analyses (Soman et al., 2010; White and Ireland, 2012). (3) Zircon can also be altered and re-precipitated by later hydrothermal fluids (Geisler et al., 2007), and hence the U-Pb ages of hydrothermally altered zircon constrain the timing of late-stage fluid processes rather than the emplacement/crystallization of the pegmatite (Wang et al., 2007; Soman et al., 2010). The U-Pb ages of Types 2 and 3 zircons from the G2 pegmatite provide a good example illustrating how zircons can be affected by post-magmatic hydrothermal alteration.

In contrast, columbite shows no evidence of inheritance or hydrothermal overprinting (Figs. 5 and 7). The textural data indicate that they are unequivocally of magmatic origin (Figs. 5A-C). The columbite U-Pb age (143 ± 1 Ma) is consistent with that of Type 2 zircons, providing a reliable constraint on the crystallization age of the pegmatite dike. The age is also consistent with the Wenyu monzogranite pluton (141 ± 2 Ma; Li et al., 2012a). The age compatibility and the close spatial relationship between the G2 pegmatite dikes and the pluton (Fig. 2), indicate that the pegmatites may have been derived from a differentiated monzogranitic magma.

Previous studies have demonstrated that U-Pb systematics of columbite can survive upper greenschist to lower amphibolite facies metamorphic conditions (Romer and Wright, 1992), as well as intense chemical weathering (Romer and Lehmann, 1995). Meanwhile, inherited components from the source region are commonly absent in columbite (e.g. Romer and Wright, 1992; Romer and Smeds, 1994; Romer and Smeds, 1997; Melcher et al., 2008). Therefore, columbite U-Pb dating provides a more robust geochronometer for dating pegmatites compared to zircon. In addition, columbite is one of the most important ore minerals in pegmatite-related Nb and Ta deposits (e.g. Černý and Ercit, 1989; Beurlen et al., 2008; Linnen et al., 2012). It also occurs widely in a range of hydrothermal deposits genetically linked to pegmatite or granite, such as Li, Be, B, and Cs deposits (e.g. Černý and Lenton, 1995; Selway et al., 2005). It is also common in Sn and W deposits (e.g. Zhang et al., 2003; Lerouge et al., 2007), and REEs deposits (e.g. Zhang et al., 2001). Thus, columbite U-Pb dating can also be used to precisely constrain the timing and history of such ore deposits.

7. Conclusions

Columbite grains from a pegmatite dike in the Xiaoqinling district, North China Craton yield concordant U-Pb ages with a weighted mean $^{206}Pb/^{238}U$ age of 143 ± 1 Ma. Textures and geochemical data confirm that the columbite was crystallized from pegmatitic magma and thus the U-Pb age provides a good constraint on the time of pegmatite formation. In contrast, zircons from the same dike consist of inherited (Type 1), syn-magmatic (Type 2), and hydrothermally altered (Type 3) varieties, which yield distinct ages of 1879 ± 30 Ma, 143 ± 1 Ma, and 127 ± 3 Ma, respectively. Morphological, textural, and geochemical data indicate that Type 2 zircons are magmatic minerals formed during pegmatite crystallization, whereas Type 3 zircons reflect post-pegmatite hydrothermal alteration presumably related to the pervasive gold mineralization in the Xiaoqinling district. This study shows that columbite can be a more robust U-Pb geochronolometer than zircon for precisely dating pegmatites and associated ore deposits. The results presented here also demonstrate that trace element geochemistry of zircon and columbite may provide information useful in distinguishing their origins, and thus the interpretation of U-Pb age data of these minerals.

Acknowledgements: We thank Zhang Suxin, Yang Meijun, and Zheng Shu for their help in SEM, EMP, and CL analysis, respectively. This research was supported by the Natural Science Foundation of China (grant 90814004), the Fundamental Research Funds for the Central Universities (CUG120102), and the MOST special fund from GPMR lab (MSFGPMR201205).

References:

Beurlen, H., Da Silva, M., Thomas, R., Soares, D., and Olivier, P., 2008. Nb-Ta-(Ti-Sn) oxide mineral chemistry as tracer of rare-element granitic pegmatite fractionation in the Borborema Province, Northeastern Brazil. Mineralium Deposita, 43(2): 207-228.

Bi, S.J., Li, J.W., and Li, Z.K., 2011. Geological significance and geochronology of Paleoproterozoic mafic dykes of the Xiaoqinling gold district, southern margin of the North China Craton. Earth Science-Journal of China University of Geosciences, 36(1): 17-31 (in Chinese with English abstract).

Černý, P., 1989.Characteristics of pegmatite deposits of tantalum, in: Möller, P., Černý, F., Saupé F. (Eds.), Lanthanides, tantalum and niobium. Springer, Berlin, pp. 195-239.

Černý, P., Roberts, W.L., Ercit, T.S., and Chapman, R., 1985. Wodginite and associated oxide minerals from the Peerless pegmatite, Pennington County, South Dakota. American Mineralogist, 70(9-10): 1044-1049.

Černý, P., Goad, B.E., Hawthorne, F.C., and Chapman R., 1986. Fractionation trends of the Nb- and Ta-bearing oxide minerals in the Greer Lake pegmatitic granite and its pegmatite aureole, southeastern Manitoba. American Mineralogist, 71(3-4): 501-517.

Černý, P., and Ercit, T.S., 1989. Mineralogy of niobium and tantalum; crystal chemical relationships, paragenetic aspects and their economic implications, in: Möller, P., Černý, F., Saupé F. (Eds.), Lanthanides, Tantalum and Niobium. Springer, Berlin, pp. 27-79.

Černý, P., and Lenton, P.G., 1995. The Buck and Pegli lithium deposits, southeastern Manitoba: the problem of updip fractionation in subhorizontal pegmatite sheets. Economic Geology, 90: 658-675

Ercit, T.S., 1994. The geochemistry and crystal chemistry of columbite-group minerals from granitic pegmatites, southwestern Grenville Province, Canadian Shield. The Canadian Mineralogist, 32(2): 421-438.

Geisler, T., Pidgeon, R.T., van Bronswijk, W., and Kurtz R., 2002. Transport of uranium, thorium, and lead in metamict zircon under low-temperature hydrothermal conditions. Chemical Geology, 191(1-3): 141-154.

Geisler, T., Schaltegger, U., and Tomaschek, F., 2007. Re-equilibration of zircon in aqueous fluids and melts. Elements, 3(1): 43-50.

Ghosh, A.K., Frei, R., and Whitehouse, M.J., 2008. U-Pb geochronologic study of magmatic zircon in Paleoproterozoic granitic pegmatite and associated metapelites, Black Hills, South Dakota: Implications for gold petrogenesis and sedimentary provenance. Geological Society of America Abstracts with Programs, 40(6): 145.

Graupner, T., Melcher, F., Gäbler, H.E., Sitnikova, M., Brätz, H., and Bahr, A., 2010. Rare earth element geochemistry of columbite-group minerals: LA-ICP-MS data. Mineralogical Magazine, 74(4): 691-713.

Hanchar, J.M., and Watson, E.B., 2003. Zircon saturation thermometry. Reviews in Mineralogy and Geochemistry, 53(1): 89-112.

Hoskin, P.W.O., 2005. Trace-element composition of hydrothermal zircon and the alteration of Hadean zircon from the Jack Hills, Australia. Geochimica et Cosmochimica Acta, 69(3): 637-648.

Hoskin, P.W.O., and Schaltegger U., 2003. The composition of zircon and igneous and metamorphic petrogenesis. Reviews in Mineralogy and Geochemistry, 53: 27-62.

Hu, S.X., and Lin, Q.L., 1989. Geology and prospecting on the collided zone between North China paleo-plate and South China paleo-plate. Nanjing University Press, Nanjing, pp. 29-35 (in Chinese).

Hu, Z.C., Gao, S., Liu, Y.S., Hu, S.H., Chen, H.H., and Yuan, H.L., 2008. Signal enhancement in laser ablation ICP-MS by addition of nitrogen in the central channel gas. Journal of Analytical Atomic Spectrometry, 23(8): 1093-1101.

Jackson, S.E., Pearson, N.J., Griffin, W.L., and Belousova, E.A., 2004. The application of laser ablation inductively coupled plasma-mass spectrometry to in situ U-Pb zircon geochronology. Chemical Geology, 211(1-2): 47-69.

Keppler, H., and Wyllie, P.J., 1990. Role of fluids in transport and fractionation of uranium and thorium in magmatic processes. Nature, 348: 531-533.

Kusiak, M.A., Dunkley, D.J., Słaby, E., Martin, H., and Budzyń, B., 2009. Sensitive high-resolution ion microprobe analysis of zircon reequilibrated by late magmatic fluids in a hybridized pluton. Geology, 37(12): 1063-1066.

Lerouge, C., Deschamps, Y., Piantone, P., Gilles, C., and Breton, J., 2007. Metal-carrier accessory minerals associated with W ± Sn mineralization, La Châtaigneraie tungsten ore district, Massif Central, France. The Canadian Mineralogist, 45(4): 875-889.

Li, S.M., Qu, L.Q., and Su, Z.B., 1996. Geology Of Gold Deposits In The Xiaoqinling District And Metallogenic Prognosis. Geological Publishing House, Beijing. 250 p (in Chinese).

Li, H.M., Chen, Y.C., Wang, D.H., Ye, H.S., Wang, Y.B., Zhang, C.Q., and Dai, J.Z., 2007. SHRIMP U-Pb zircon ages of metamorphic rocks and veins in the Xiaoqinling area, Henan, and their geological significance. Acta Petrologica Sinica, 23(10): 2504-2512 (in Chinese with English abstract).

Li, J.W., Deng, X.D., Zhou, M.F., Liu, Y.S., Zhao, X.F., and Guo, J.L., 2010. Laser ablation ICP-MS titanite U-Th-Pb dating of hydrothermal ore deposits: A case study of the Tonglushan Cu-Fe-Au skarn deposit, SE Hubei Province, China. Chemical Geology, 270(1-2): 56-67.

Li, J.W., Li, Z.K., Zhou, M.F., Chen, L., Bi, S.J., Deng, X.D., Qiu, H.N., Cohen, B., Selby, D., and Zhao, X.F., 2012a. The early Cretaceous Yangzhaiyu lode gold deposit, North China Craton: a link between craton reactivation and gold veining. Economic Geology, 107(1): 43-79.

Li, J.W., Bi, S.J., Selby, D., Chen, L., Vasconcelos, P., Thiede, D., Zhou, M.F., Zhao, X.F., Li, Z.K., and Qiu, H.N., 2012b. Giant Mesozoic gold provinces related to the destruction of the North China craton. Earth and Planetary Science Letters, 349-350: 26-37.

Linnen, R.L., and Keppler, H., 1997. Columbite solubility in granitic melts; consequences for the enrichment and fractionation of Nb and Ta in the Earth's crust. Contributions to Mineralogy and Petrology, 128(2-3): 213-227.

Linnen, R.L., Van Lichtervelde, M., and Černý, P., 2012. Granitic pegmatites: granitic pegmatites as sources of strategic metals. Elements, 8: 275-280.

Liu, Y.S., Hu, Z.C., Gao, S., Günther, D., Xu, J., Gao, C.G., and Chen, H.H., 2008. In situ analysis of major and trace elements of anhydrous minerals by LA-ICP-MS without applying an internal standard. Chemical Geology, 257(1-2): 34-43.

Liu, Y., Hu, Z., Zong, K., Gao, C., Gao, S., Xu, J., and Chen, H., 2010a. Reappraisement and refinement of zircon U-Pb isotope and trace element analyses by LA-ICP-MS. Chinese Science Bulletin, 55(15): 1535-1546.

Liu, Y.S., Gao, S., Hu, Z.C., Gao, C.G., Zong, K.Q., and Wang, D.B., 2010b. Continental and oceanic crust recycling-induced melt-peridotite interactions in the Trans-North China Orogen: U-Pb Dating, Hf isotopes and trace elements in zircons from mantle xenoliths. Journal of Petrology, 51(1-2): 537-571.

London, D., 2005. Granitic pegmatites; an assessment of current concepts and directions for the future. Lithos, 80(1): 281-303.

Ludwig, K.R., 2003. ISOPLOT 3.00: A geochronological toolkit for Microsoft Excel. Berkeley Geochronology Center, California, Berkeley.

Mao, J.W., Xie, G.Q., Pirajno, F., Ye, H.S., Wang, Y.B., Li, Y.F., Xiang, J.F., and Zhao, H.J., 2010. Late Jurassic–Early Cretaceous granitoid magmatism in Eastern Qinling, central-eastern China: SHRIMP zircon U–Pb ages and tectonic implications. Australian Journal of Earth

Sciences, 57(1): 101-112.

Marsh, J.H., Gerbi, C.C., Culshaw, N.G., Johnson, S.E., Wooden, J.L., and Clark, C., 2012. Using zircon U-Pb ages and trace element chemistry to constrain the timing of metamorphic events, pegmatite dike emplacement, and shearing in the southern Parry Sound domain, Grenville Province, Canada. Precambrian Research, 192-195(0): 142-165.

Melcher, F., Sitnikova, M.A., Graupner, T., Martin, N., Oberthür, T., Henjes-Kunst, F., Gäbler, E., Gerdes, A., Brätz, H., Davis, D.W., and Dewaele, S., 2008. Fingerprinting of conflict minerals: columbite-tantalite ("coltan") ores. SGA News, 23: 1-14.

Möller, P., 1989. REE(Y), Nb, and Ta enrichment in pegmatites and carbonatite-alkalic rock complexes, in: Möller, P., Černý, F., Saupé F. (Eds.), Lanthanides, Tantalum and Niobium. Springer, Berlin, pp. 103-144.

Nie, F.J., Jiang, S.H., and Zhao, Y.M., 2001. Lead and sulfur isotopic studies of the Wenyu and the Dongchuang quartz vein type gold deposits in the Xiaoqinling area, Henan and Shaanxi Provinces, Central China. Mineral Deposits, 20: 163-173 (in Chinese with English abstract).

Pupin, J.P., 2000. Granite genesis related to geodynamics from Hf-Y in zircon. Transactions of the Royal Society of Edinburgh: Earth Sciences, 91(1-2): 245-256.

Romer, R.L., 1997. U-Pb age of rare-element pegmatites at Stora Vika, SE Sweden. GFF, 119(4): 291-294.

Romer, R.L., and Lehmann, B., 1995. U-Pb columbite age of Neoproterozoic Ta-Nb mineralization in Burundi. Economic Geology, 90(8): 2303-2309.

Romer, R.L., and Smeds, S.A., 1994. Implications of U-Pb ages of columbite-tantalites from granitic pegmatites for the Palaeoproterozoic accretion of 1.90-1.85 Ga magmatic arcs to the Baltic Shield. Precambrian Research, 67(1-2): 141-158.

Romer, R.L., and Smeds, S.A., 1996. U-Pb columbite ages of pegmatites from Sveconorwegian terranes in southwestern Sweden. Precambrian Research, 76(1-2): 15-30.

Romer, R.L., and Smeds, S.A., 1997. U-Pb columbite chronology of post-kinematic Palaeoproterozoic pegmatites in Sweden. Precambrian Research, 82(1-2): 85-99.

Romer, R.L., and Wright, J.E., 1992. U-Pb dating of columbites; a geochronologic tool to date magmatism and ore deposits. Geochimica et Cosmochimica Acta, 56(5): 2137-2142.

Rubatto, D., 2002. Zircon trace element geochemistry: partitioning with garnet and the link between U-Pb ages and metamorphism. Chemical Geology, 184(1-2): 123-138.

Selway, J.B., Breaks, F.W., Tindle, A.J., 2005. A review of rare-element (Li-Cs-Ta) pegmatite exploration techniques for the Superior Province, Canada, and large worldwide tantalum deposits. Exploration and Mining Geology, 14(1-4): 1-30

Simmons, W.B., Pezzotta, F., Shigley, J.E., and Beurlen, H., 2012. Granitic pegmatites: granitic pegmatites as sources of colored gemstones. Elements, 8: 281-287.

Smith, S.R., Foster, G.L., Romer, R.L., Tindle, A.G., Kelley, S.P., Noble, S.R., Horstwood, M., and Breaks, F.W., 2004. U-Pb columbite-tantalite chronology of rare-element pegmatites using TIMS and laser ablation-multi collector-ICP-MS. Contributions to Mineralogy and Petrology, 147(5): 549-564.

Soman, A., Geisler, T., Tomaschek, F., Grange, M., and Berndt, J., 2010. Alteration of crystalline zircon solid solutions: a case study on zircon from an alkaline pegmatite from Zomba–Malosa, Malawi. Contributions to Mineralogy and Petrology, 160(6): 909-930.

Stacey, J.S., and Kramers, J.D., 1975. Approximation of terrestrial lead isotope evolution by a two-stage model. Earth and Planetary Science Letters, 26(2): 207-221.

Storey, C.D., Jeffries, T.E., and Smith, M., 2006. Common lead-corrected laser ablation ICP-MS U-Pb systematics and geochronology of titanite. Chemical Geology, 227(1-2): 37-52.

Wang, T., Tong, Y., Jahn, B.M., Zou, T.R., Wang, Y.B., Hong, D.W., and Han, B.F., 2007. SHRIMP U-Pb Zircon geochronology of the Altai No. 3 Pegmatite, NW China, and its implications for the origin and tectonic setting of the pegmatite. Ore Geology Reviews, 32(1-2): 325-336.

Wang, T.H., Mao, J.W., and Wang, Y.B., 2008. Research on SHRIMP U-Pb chronology in Xiaoqinling-Xionger' shan area: evidence of delamination of lithosphere in the Qinling orogenic belt. Acta Petrologica Sinica, 24(6): 1273-1287 (in Chinese with English abstract).

Watson, E.B., and Harrison, T.M., 1983. Zircon saturation revisited: temperature and composition effects in a variety of crustal magma types. Earth and Planetary Science Letters, 64(2): 295-304.

White, L.T., and Ireland, T.R., 2012. High-uranium matrix effect in zircon and its implications for SHRIMP U-Pb age determinations. Chemical Geology, 306-307(0): 78-91.

Wiedenbeck, M., Allé, P., Corfu, F., Griffin, W.L., Meier, M., Oberli, F., Quadt, A.V., Roddick, J.C., and Spiegel, W., 1995. Three natural zircon standards for U-Th-Pb, Lu-Hf, trace element and REE analyses. Geostandards Newsletter, 19(1): 1-23.

Xu, X., Griffin, W., Ma, X., O’Reilly, S., He, Z., and Zhang, C., 2009. The Taihua group on the southern margin of the North China craton: further insights from U–Pb ages and Hf isotope compositions of zircons. Mineralogy and Petrology, 97(1): 43-59.

Zhang, W.L., Hua, R.M., and Wang, R.C., 2003. Intergrowth of wolframoixiolite and W-rich manganocolumbite in the Dajishan tungsten deposit, Jiangxi Province, South China. Mineral Deposits, 22(2): 158-165 (in Chinese with English abstract).

Zhang, P.S., Tao, K.J., Yang, Z.M., Yang, X.M., Song, R.K., 2001. Genesis of rare earths, niobium and tantalum minerals in the Bayan Obo ore deposit of China. Journal of the Chinese Rare Earth Society, 19(2): 97-102 (in Chinese with English abstract).

Figure and table captions

Figure 1. Simplified geological map of the Xiaoqinling district (modified from Li et al., 1996).

Figure 2. Map showing distribution of the G1 and G2 pegmatite dikes around the Wenyu monzogranite pluton.

Figure 3. Photograph (A) and sketch map (B) showing the pegmatite dikes used for this study.

Figure 4. Photograph (A) and photomicrograph (B) showing mineralogical and textural features of a G2 pegmatite used for geochemical and U-Pb geochronological study. (A) G2 pegmatite typically consisting of very coarse-grained albite intergrown with medium-grained quartz, muscovite, biotite, and garnet; (B) hydrothermal sericite in albite.

Figure 5. BSE images showing the composition and textural features of columbite in the G2 pegmatite. (A-C) columbite included in quartz, albite, and garnet. Other accessory minerals in equilibration with garnet include zircon, monazite, and thorite. (D) compositionally and texturally homogeneous columbite. Mineral abbreviations: Ab-albite; Bt-biotite; Col-columbite; Grt-garnet; Ms-muscovite; Moz-monazite; Qz-quartz; Ser-sericite; Thr-thorite; Zr-zircon.

Figure 6. (A) Ta/(Nb+Ta) *vs* Mn/(Mn+Fe) diagram for columbite-group minerals (modified from Černý and Ercit, 1985); (B) (Nb+Ta)-(Fe+Mn)-(Ti+Sn+U+Zr+Sc) (atomic ratios) ternary plots of columbite from the pegmatite dike. The line denotes the ideal trend defined by the substitution: $(Fe,Mn)^{2+} + 2(Nb,Ta)^{5+} = 3(Ti+Sn+U+Zr+Sc)^{4+}$ (Černý and Ercit, 1985).

Figure 7. Plots showing geochemical characteristics of columbite from the pegmatite dike. (A-D) positive correlations of Ti *vs* Sn, U, Sc, and Zr; (E) tetravalent cations (Ti+Sn+U+Zr+ Sc) *vs* Ta/(Ta+Nb) diagram showing a general negative correlation; (F) a positive correlation

between W and Ta; (G) well positive correlation between U and Th; (H) Positive correlation between U and REEs; (I) chondrite-normalized REE patterns of columbite.

Figure 8. BSE (A, C, E) and CL (B, D) images showing the morphological and textural features of zircons. (A, B) Homogeneous Type 1 zircon with oscillatory zoning; (C, D) Homogeneous and inclusion-free Type 2 zircon with dark CL image; (E) Typical Type 3 zircon with abundant micrometer-sized pores and mineral inclusions, thorite (Thr) and uranium oxides (UO_X) in this case.

Figure 9. Plots showing geochemical characteristics of three types of zircons from the pegmatite dike. (A-D) correlation between Ca and P, Ti, Nb/Ta, and Th/U showing increase of the “non-formula” elements in zircons due to alteration; (E-F) correlation of LREE/HREE *vs* LREE/MREE (E) and LREE/HREE *vs* MREE/HREE (F) showing distributions of HREE, MREE, and LREE in zircons; (G) chondrite-normalized REE patterns of zircons; (H, I) cerium anomaly (Ce*) *vs* $(Sm/La)_N$ and $(Sm/La)_N$ *vs* La diagrams. The reference areas of magmatic and hydrothermal zircons are after Hoskin (2005).

Figure 10. LA-ICPMS U-Pb concordia plots of columbite (A) and zircon (B) from the G2 pegmatite dike under investigation. Age uncertainties are quoted as 95% confidence level (2σ), individual precision ellipses are 1σ.

Table 1. Electron microprobe data of columbite from the G2 pegmatite.

Table 2. Trace element data of columbite by LA-ICP-MS analyses.

Table 3. Trace element data of zircon by LA-ICP-MS analyses.

Table 4. LA-ICPMS U-Pb isotope data for columbites and zircons from the G2 pegmatite.

Supplementary Table S.1. Major element data of the G2 pegmatite.

Supplementary Table S.2. Trace element data of the G2 pegmatite.

Figure
Click here to download high resolution image

Deng et al., Figure 1

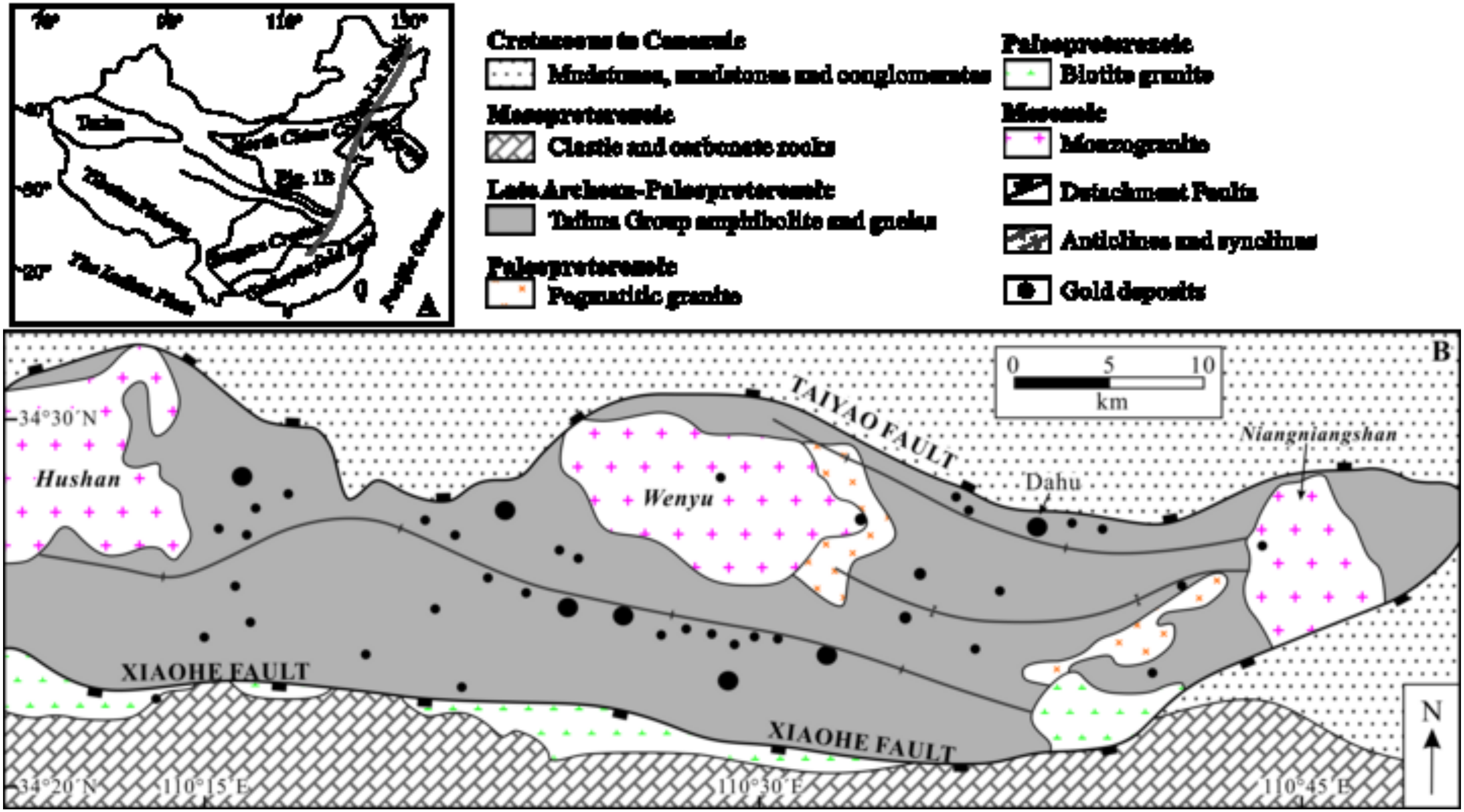

Figure 2
Click here to download high resolution image

Deng et al., Figure 2

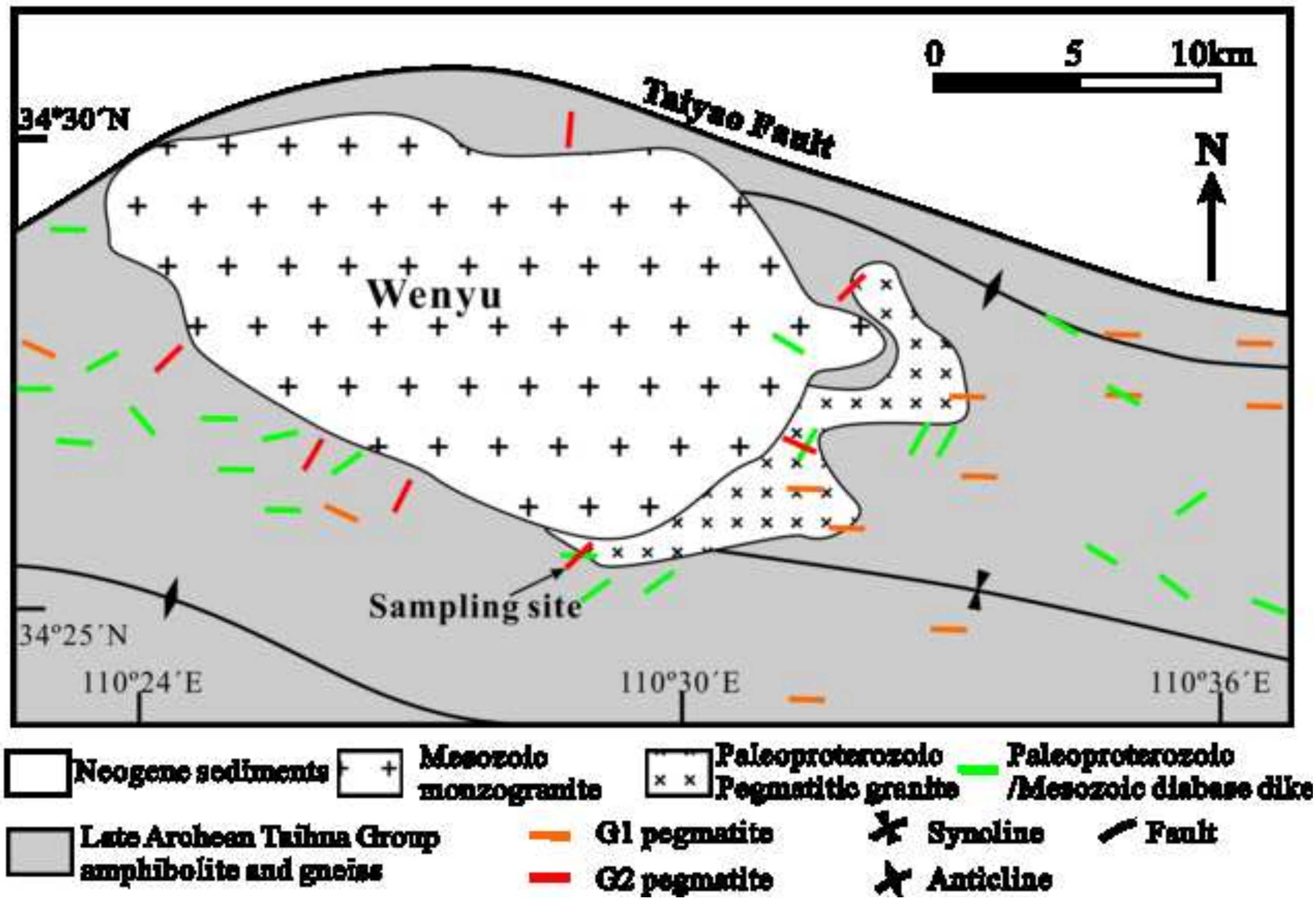

Figure 3
Click here to download high resolution image

Deng et al., Figure 3

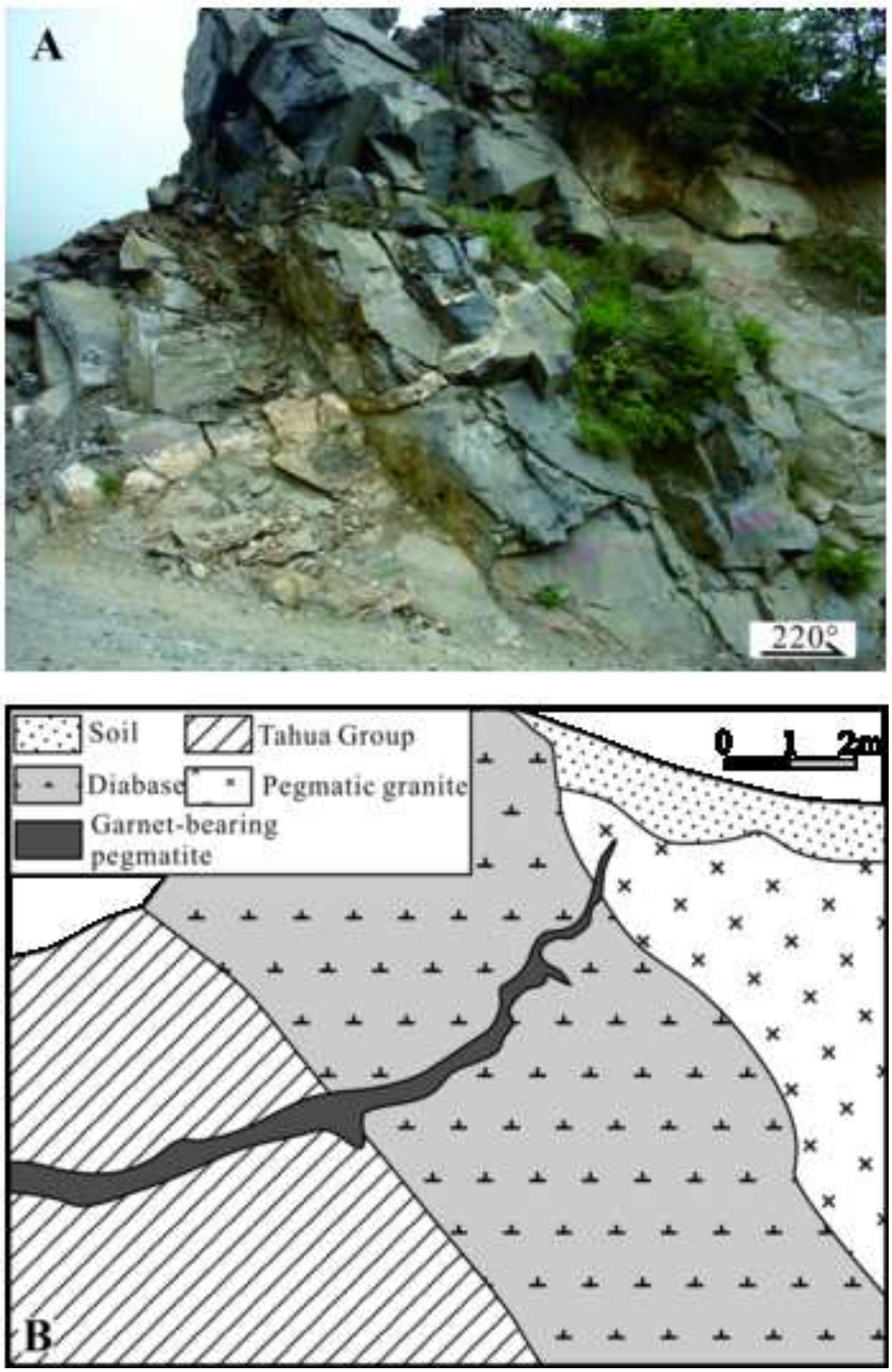

Figure 4
Click here to download high resolution image

Deng et al., Figure 4

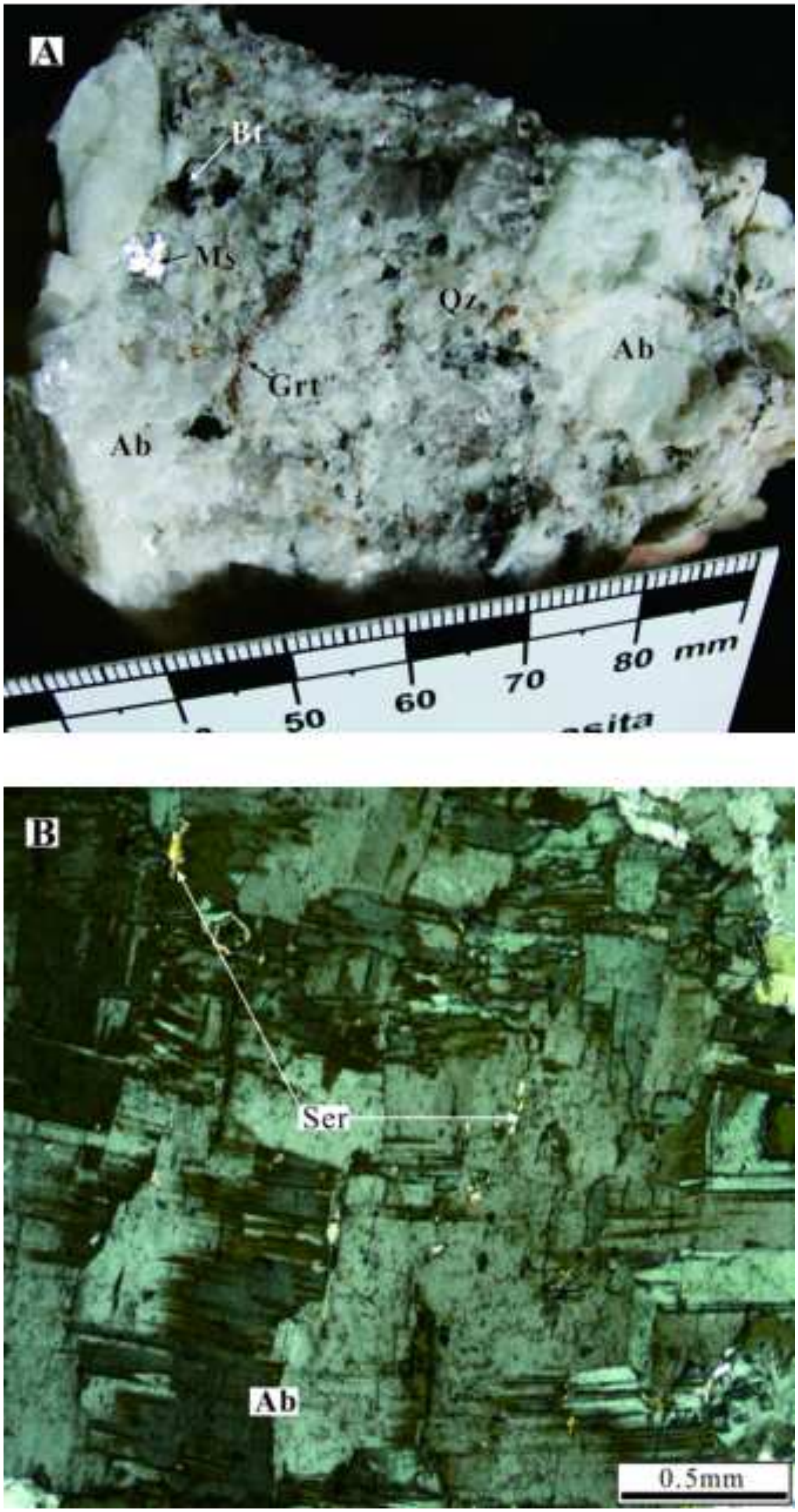

Figure 5
Click here to download high resolution image

Deng et al., Figure 6

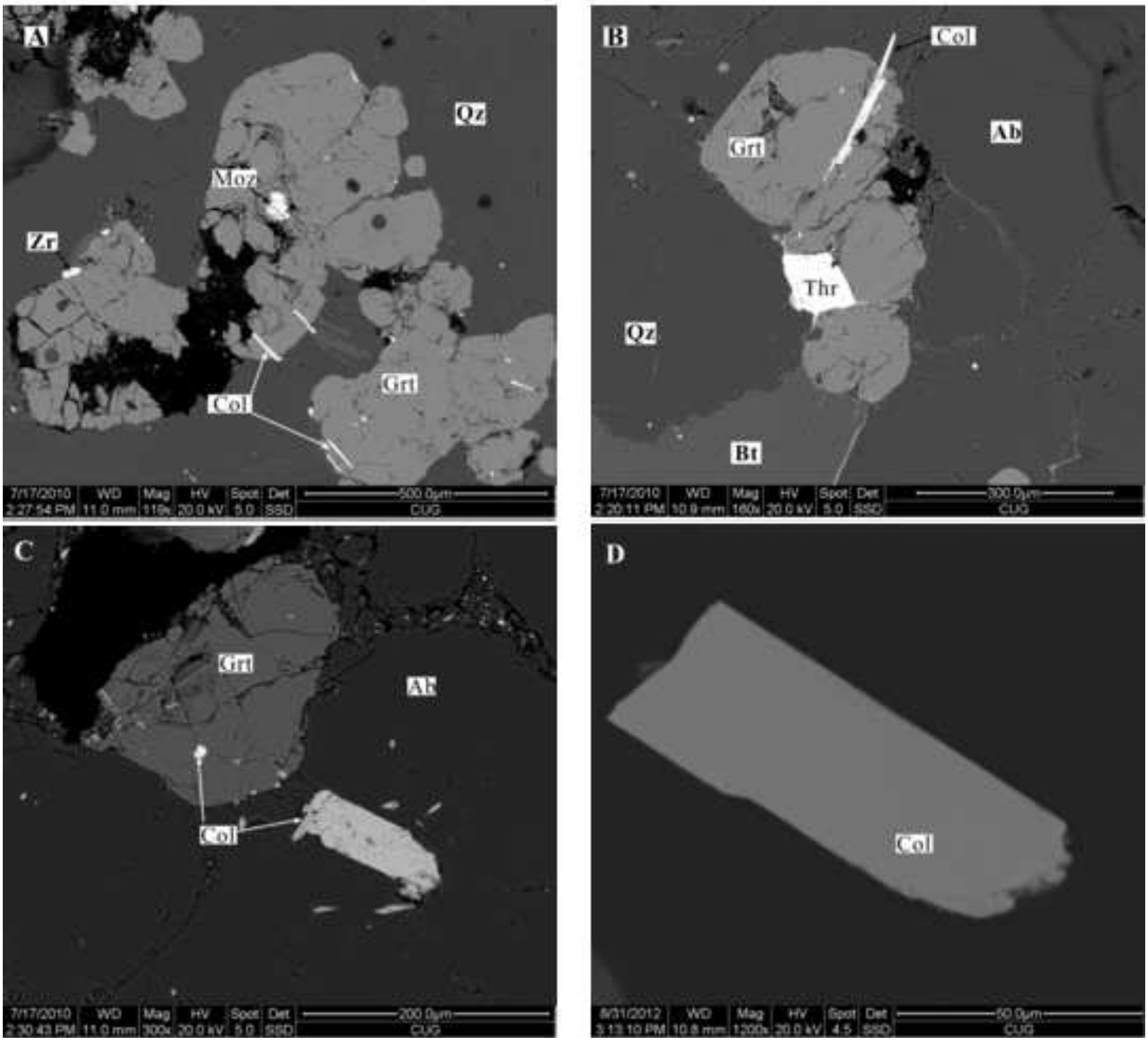

Figure 6
Click here to download high resolution image

Deng et al., Figure 6

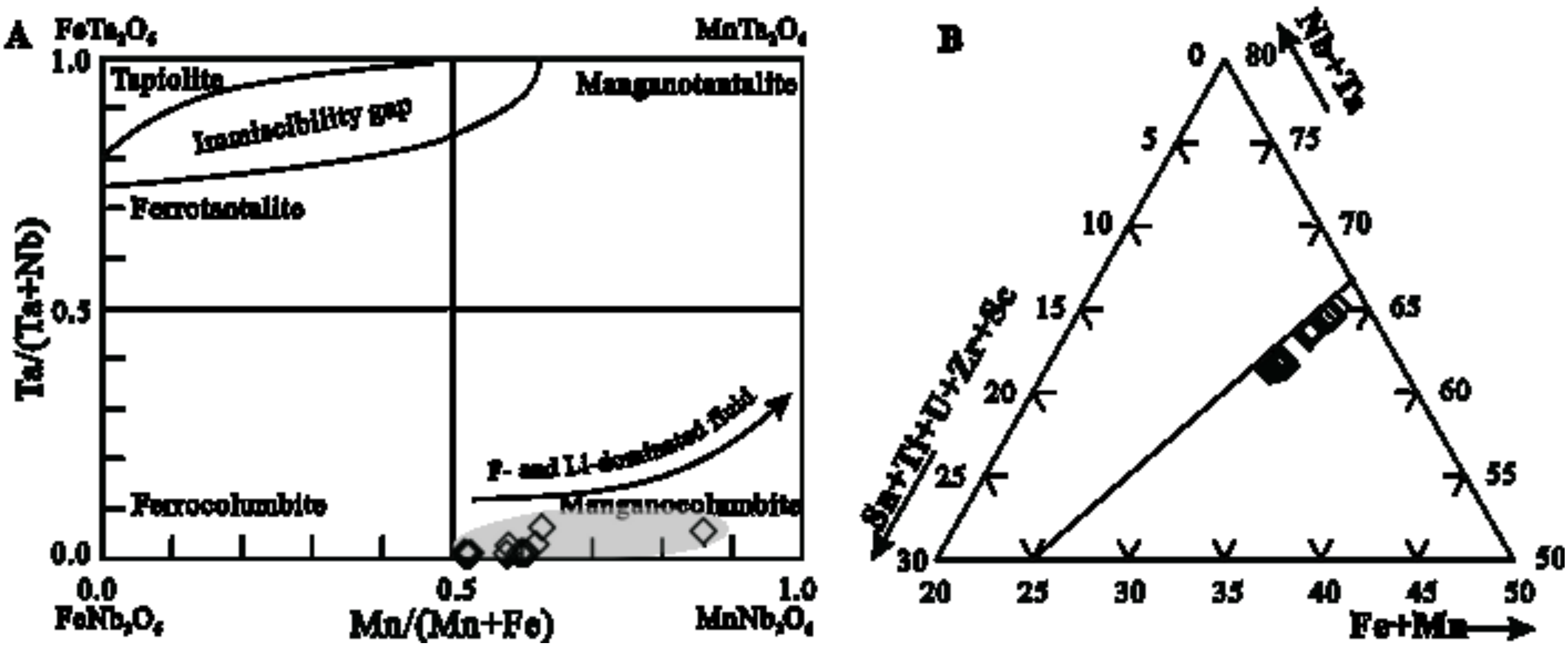

Figure 7

Click here to download high resolution image

Deng et al., Figure 7

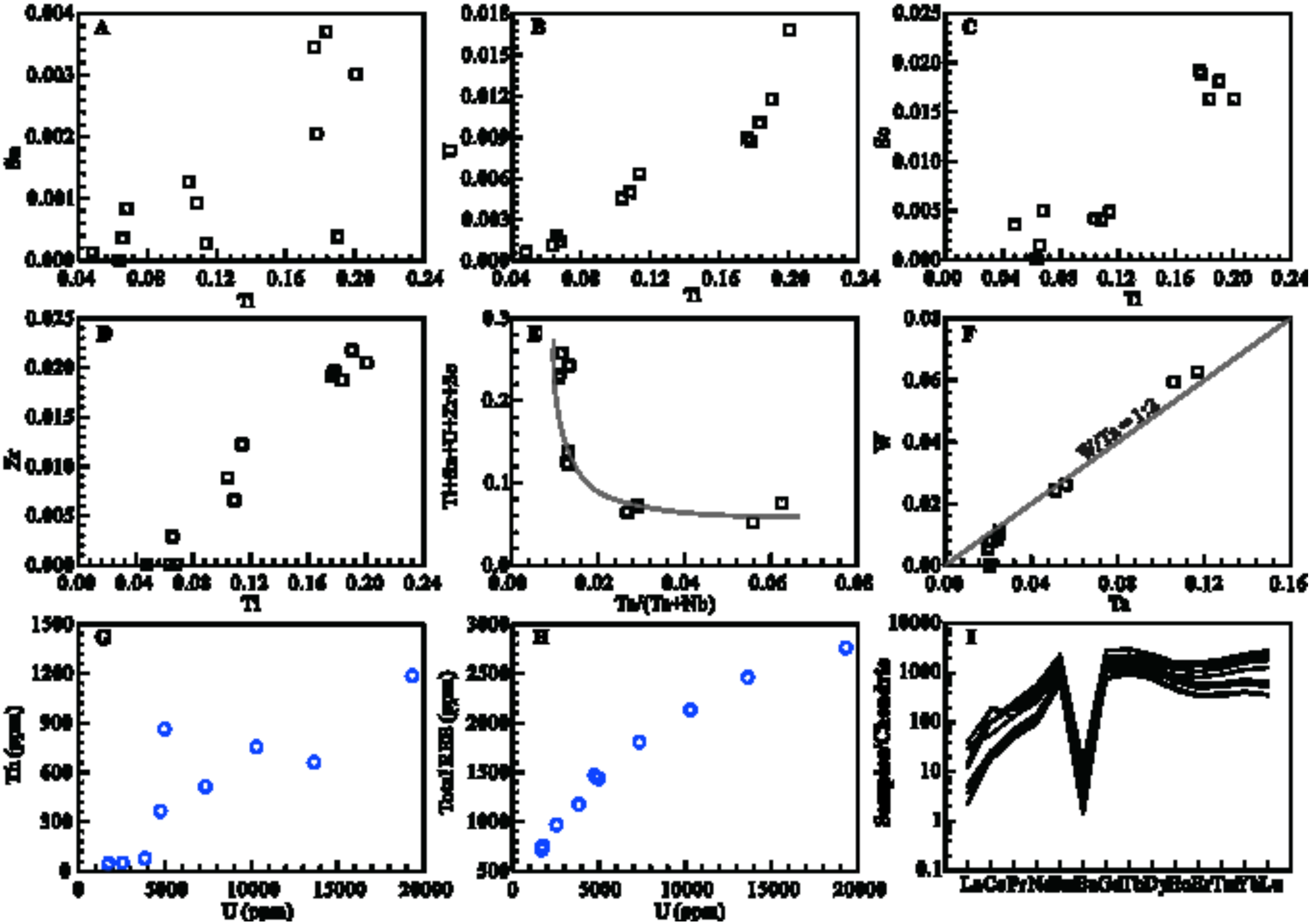

Figure 8
Click here to download high resolution image

Deng et al., Figure 8

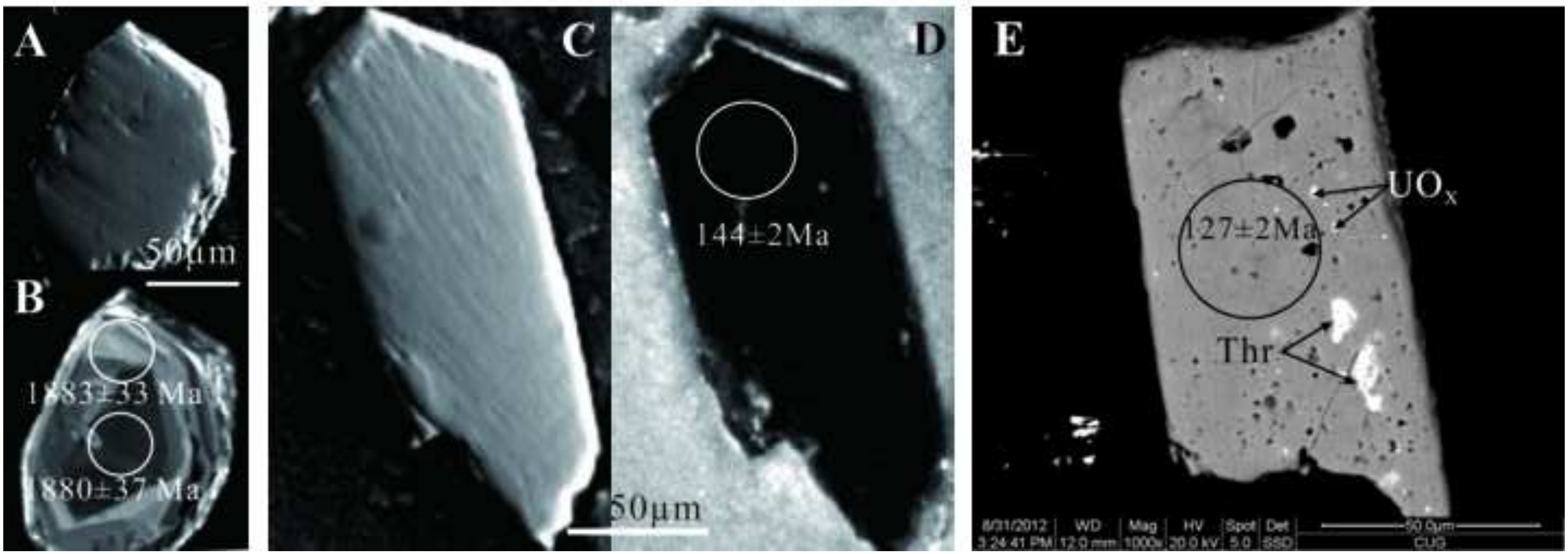

Figure 9

Click here to download high resolution image

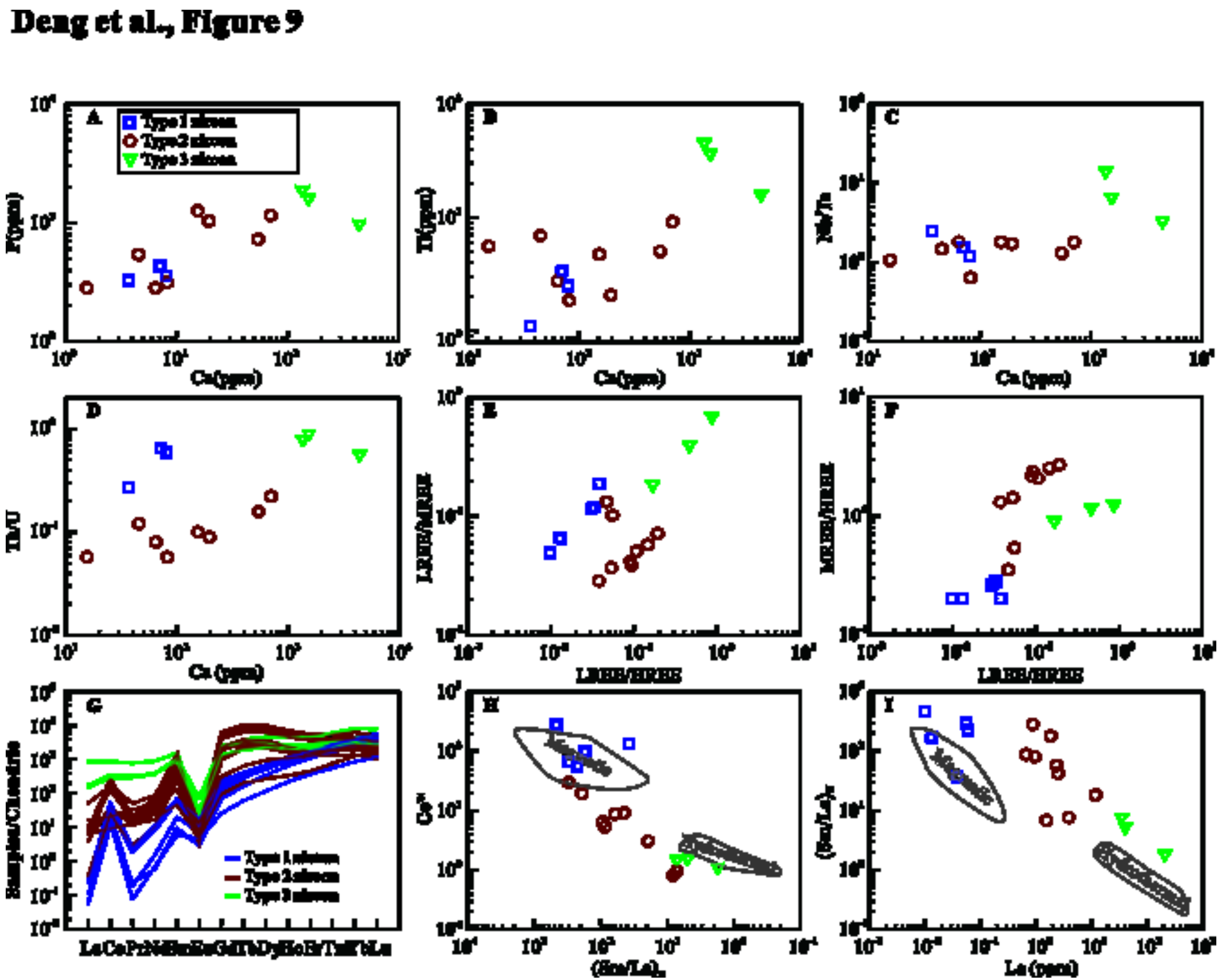

Figure 10
Click here to download high resolution image

Deng et al., Figure 10

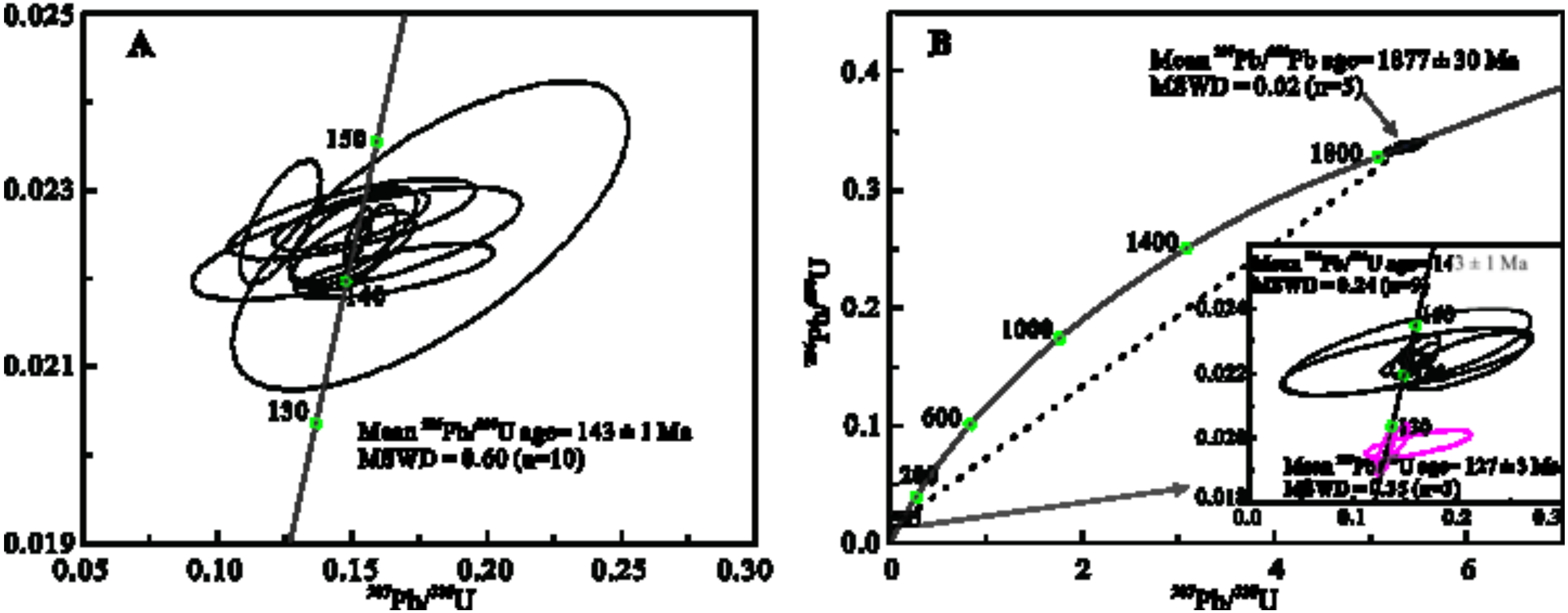

Table 1

Click here to download Table: Table 1 Major elements Columbite.xls

Table 1. Electron microprobe analyses (wt.%) of columbite from the Wenyu G2 pegmatit

Sample	1#-1	1#-2	2#-1	2#-2	3#-1	3#-2	4#-1	4#-2	4#-3
CaO	0.00	0.00	0.00	0.00	0.00	0.00	0.00	0.00	0.00
FeO	2.87	7.50	7.90	8.76	9.70	9.47	8.18	8.23	8.30
MnO	17.17	12.50	12.67	11.95	10.27	10.38	12.41	12.34	12.12
TiO2	1.12	1.58	1.56	1.50	4.50	4.76	2.48	2.59	2.70
Nb2O5	69.25	68.13	72.80	72.98	69.92	70.24	73.85	73.96	73.00
Ta2O5	6.81	7.56	3.66	3.33	1.57	1.38	1.63	1.60	1.60
SnO2	0.01	0.04	0.02	0.00	0.02	0.14	0.06	0.04	0.01
WO3	4.02	4.26	1.81	1.67	0.56	0.53	0.76	0.65	0.68
UO2	0.05	0.11	0.14	0.09	0.94	1.35	0.37	0.40	0.51
ZrO2	0.00	0.00	0.11	0.00	0.79	0.75	0.33	0.24	0.45
Y2O3	0.35	0.63	1.09	1.15	1.06	0.75	1.26	1.17	1.08
Sc2O3	0.07	0.10	0.03	0.00	0.37	0.34	0.09	0.09	0.10
Total	101.70	102.42	101.76	101.43	99.69	100.09	101.41	101.31	100.56
Ca	0.000	0.000	0.000	0.000	0.000	0.000	0.000	0.000	0.000
Fe	0.137	0.357	0.370	0.412	0.456	0.444	0.380	0.383	0.389
Mn	0.831	0.603	0.602	0.569	0.490	0.493	0.585	0.581	0.575
Ti	0.048	0.068	0.066	0.063	0.190	0.201	0.104	0.108	0.114
Nb	1.788	1.753	1.847	1.855	1.779	1.779	1.857	1.859	1.849
Ta	0.106	0.117	0.056	0.051	0.024	0.021	0.025	0.024	0.024
Sn	0.000	0.001	0.000	0.000	0.000	0.003	0.001	0.001	0.000
W	0.059	0.063	0.026	0.024	0.008	0.008	0.011	0.009	0.010
U	0.001	0.001	0.002	0.001	0.012	0.017	0.005	0.005	0.006
Zr	0.000	0.000	0.003	0.000	0.022	0.021	0.009	0.007	0.012
Y	0.011	0.019	0.032	0.034	0.032	0.022	0.037	0.035	0.032
Sc	0.004	0.005	0.001	0.000	0.018	0.016	0.004	0.004	0.005
Total	2.984	2.987	3.006	3.010	3.031	3.024	3.017	3.016	3.018
Mn/(Mn+Fe)	0.859	0.628	0.619	0.580	0.518	0.526	0.606	0.603	0.597
Ta/(Ta+Nb)	0.056	0.063	0.029	0.027	0.013	0.012	0.013	0.013	0.013

Table 2
Click here to download Table: Table 2 Columbite Trace elements.xls

Table 2. Trace element analyses (ppm) of columbite by the LA-ICP-MS.

Spot no.	WY08-1	WY08-2	WY08-3	WY08-4	WY08-5	WY08-6	WY08-7	WY08-8	WY08-9
La	0.56	1.31	6.94	3.05	3.70	7.06	9.71	0.90	1.23
Ce	11.8	16.0	35.2	62.8	113	60.3	114	10.8	12.4
Pr	5.18	6.86	12.7	24.8	12.6	20.4	17.1	4.63	4.76
Nd	57.8	70.9	125	272	139	213	164	44.9	49.1
Sm	106	133	155	352	173	243	204	91.9	88.1
Eu	0.08	0.16	0.40	0.84	0.42	0.75	0.47	0.15	0.22
Gd	211	257	273	594	310	431	352	169	158
Tb	49.2	58.8	56.2	114	63.5	85.6	73.9	41.0	36.6
Dy	271	324	323	605	385	503	439	216	196
Ho	37.6	45.6	51.7	92.7	68.7	95.2	80.0	28.3	25.8
Er	83.6	102	138	232	180	271	227	59.7	56.0
Tm	13.6	16.1	23.8	37.4	32.3	47.7	40.7	9.83	8.82
Yb	105	125	201	318	278	410	348	71.7	69.2
Lu	13.6	16.8	32.6	51.5	46.6	70.8	60.1	9.37	9.08
Hf	461	644	571	805	673	818	842	364	340
Pb	63.8	121.9	224	490.0	294	690	424	58.4	62.3
Th	50.6	79.2	863	1186	514	661	755	49.2	36.7
U	2561	3852	4988	19314	7356	13630	10303	1763	1713

Table 3
Click here to download Table: Table 3 Zircon Trace elements.xls

Table 3. Trace element analyses (ppm) of zircon by LA-ICP-MS.

Analysis No	WY08-101	WY08-102	WY08-103	WY08-104	WY08-105	WY08-106
			Type 1 zircons			
Li	98	121	87	60.5	73.9	53.0
P	325	860	144	355	430	1260
Ca	36.9	b.d.l.	b.d.l.	80.5	71.3	155
Ti	1.10	3.18	1.90	2.51	3.34	4.75
Y	1122	1866	383	1483	1904	11216
Nb	25.4	3.20	1.18	4.12	5.31	128
La	0.01	0.01	0.04	0.06	0.05	1.86
Ce	6.91	15.2	9.1	23.4	31.5	161
Pr	0.022	0.018	0.007	0.17	0.24	1.95
Nd	0.27	0.70	0.32	3.79	5.24	35.8
Sm	1.45	2.99	0.91	8.8	10.5	230
Eu	0.16	0.42	0.27	0.61	1.06	0.62
Gd	14.0	25.4	5.24	37.2	48.2	1293
Tb	6.17	10.52	2.27	11.3	15.4	384
Dy	86.9	144	29.4	129	173	2503
Ho	36.8	60.6	12.3	49.5	63.7	398
Er	183	289	61.3	230	288	902
Tm	41.7	69.8	14.1	50.8	64.2	140
Yb	420	715	145	519	648	1043
Lu	79.9	137	29.8	100	121	122
Hf	17711	17112	10827	11325	13628	94475
Ta	9.79	2.93	1.18	3.29	3.29	71.3
Pb	381	526	159	224	259	1552
Th	261	301	67.4	311	399	6483
U	964	1366	411	523	618	65043
LREE/MREE	0.05	0.07	0.19	0.12	0.12	0.04
LREE/HREE	0.01	0.01	0.04	0.03	0.03	0.09
MREE/HREE	0.20	0.20	0.20	0.26	0.28	2.18
Nb/Ta	2.6	1.1	1.0	1.3	1.6	1.8
$(Sm/La)_N$	169.9	462.7	37.2	227.0	295.5	191.7
Ce*	99.5	277.2	135.3	56.0	67.0	20.7
Eu*	0.111	0.147	0.376	0.103	0.144	0.003

[1] LREE = La+Ce+Pr+Nd; MREE = Sm+Eu+Gd+Tb+Dy+Ho; HREE = Er + Tm + Yb + Lu; Eu* = Eu_N/sqrt $(Sm*Gd)_N$; Ce* = Ce_N/sqrt(L

[2] Eu* = Eu_N/sqrt $(Sm*Gd)_N$; Ce* = Ce_N/sqrt$(La*Pr)_N$; $(Sm/La)_N = Sm_N/La_N$; b.d. = below detection limit.

[3] b.d.l. = below detection limit.

Table 4

Click here to download Table: Table 4 U-Pb ages of Zircon and Columbite.xls

Table 4. LA-ICP-MS U-Pb isotope data of columbite and zircon from the G2 pegmatite.

Analysis No	$^{207}Pb/^{206}Pb$	1σ	$^{207}Pb/^{235}U$	1σ	$^{206}Pb/^{238}U$	1σ	Th/U	$^{207}Pb/^{206}Pb$ (Ma)	1σ	$^{207}Pb/^{235}U$ (Ma)	1σ	$^{206}Pb/^{238}U$ (Ma)	1σ
Columbite													
WY08-1	0.0510	0.0014	0.1574	0.0059	0.0224	0.0003	0.02	239	61	148	5	143	2
WY08-2	0.0545	0.0075	0.1659	0.0243	0.0221	0.0002	0.02	391	288	156	21	141	1
WY08-3	0.0379	0.0024	0.1235	0.0099	0.0226	0.0005	0.17	-413	228	118	9	144	3
WY08-4	0.0492	0.0007	0.1523	0.0032	0.0225	0.0002	0.06	157	31	144	3	143	1
WY08-5	0.0478	0.0057	0.1496	0.0192	0.0227	0.0002	0.07	87	239	142	17	144	1
WY08-6	0.0376	0.0094	0.1518	0.0402	0.0224	0.0004	0.05	-431	364	143	35	143	3
WY08-7	0.0468	0.0048	0.1504	0.0157	0.0225	0.0004	0.07	40	201	142	14	143	2
WY08-8	0.0472	0.0089	0.1501	0.0302	0.0227	0.0003	0.03	57	312	142	27	144	2
WY08-9	0.0454	0.0102	0.1791	0.0484	0.0225	0.0012	0.02	-1	335	167	42	143	7
WY08-10	0.0486	0.0043	0.1504	0.0150	0.0223	0.0003	0.08	130	186	142	13	142	2
Zircon													
WY08-101	0.1152	0.0022	5.4094	0.1047	0.3384	0.0023	3.85	1883	33	1886	17	1879	11
WY08-102	0.1150	0.0020	5.3644	0.0958	0.3361	0.0022	4.75	1880	37	1879	15	1868	11
WY08-103	0.1147	0.0017	5.3985	0.0835	0.3386	0.0022	6.22	1876	27	1885	13	1880	11
WY08-104	0.1146	0.0024	5.3208	0.1150	0.3346	0.0026	1.72	1873	38	1872	18	1861	13
WY08-105	0.1152	0.0026	5.3492	0.1200	0.3346	0.0029	1.73	1884	41	1877	19	1861	14
WY08-106	0.0482	0.0010	0.1515	0.0036	0.0226	0.0003	0.10	109	48	143	3	144	2
WY08-107	0.0489	0.0010	0.1532	0.0035	0.0225	0.0002	0.09	142	49	145	3	143	1
WY08-108	0.0488	0.0046	0.1595	0.0154	0.0225	0.0004	0.10	139	199	150	13	144	3
WY08-109	0.0303	0.0155	0.1517	0.0776	0.0227	0.0009	0.08	-271	624	143	68	145	6
WY08-110	0.0530	0.0028	0.1679	0.0092	0.0225	0.0003	0.21	328	117	158	8	144	2
WY08-111	0.0465	0.0089	0.2058	0.0396	0.0224	0.0006	0.05	25	312	190	33	143	4
WY08-112	0.0493	0.0007	0.1529	0.0034	0.0225	0.0003	0.08	162	30	144	3	143	2
WY08-113	0.0467	0.0044	0.1502	0.0155	0.0223	0.0002	0.07	34	190	142	14	142	1
WY08-114	0.0061	0.0032	0.1508	0.0799	0.0224	0.0007	0.09	-1584	211	143	71	143	4
WY08-115	0.0470	0.0016	0.1301	0.0052	0.0195	0.0004	0.52	49	68	124	5	125	3
WY08-116	0.0522	0.0019	0.1446	0.0057	0.0200	0.0003	0.81	293	82	137	5	128	2
WY08-117	0.0534	0.0109	0.1621	0.0333	0.0198	0.0003	0.28	346	388	153	29	127	2

Supplementary Data

Click here to download Background dataset for online publication only: Supplementary Data.doc